

Mitigating information leakage in a crowded spectrum of weakly anharmonic qubits

V. Vesterinen,^{1,2} O.-P. Saira,² A. Bruno,² and L. DiCarlo²

¹*VTT Technical Research Centre of Finland, P.O. Box 1000, 02044 VTT, Finland*

²*Kavli Institute of Nanoscience, Delft University of Technology,
P.O. Box 5046, 2600 GA Delft, The Netherlands*

(Dated: February 23, 2022)

A challenge for scaling up quantum processors using frequency-crowded, weakly anharmonic qubits is to drive individual qubits without causing leakage into non-computational levels of the others, while also minimizing the number of control lines. To address this, we implement single-qubit Wah-Wah control in a circuit QED processor with a single feedline for all transmon qubits, operating at the maximum gate speed achievable given the frequency crowding. Randomized benchmarking and quantum process tomography confirm alternating qubit control with $\leq 1\%$ average error per computational step and decoherence-limited idling of one qubit while driving another with a Wah-Wah pulse train.

Experimental quantum computing [1] seldom employs true qubits. Most architectures use effective qubits defined by a pair of energy levels within a multi-level quantum object (typically the ground and first excited states, labelled $|0\rangle$ and $|1\rangle$). Examples include non-spin-1/2 electron and nuclear spins [2], electronic levels in atoms and ions [3], photons with combined polarization, frequency and positional degrees of freedom [4], and most superconducting quantum circuits [5]. The transmon [6], phase [7] and capacitively-shunted flux [8] qubits are weakly anharmonic oscillators with logical transition frequency ω_{01} and nearest leakage transition frequency ω_{12} detuned by $|\Delta| = |\omega_{12} - \omega_{01}| \sim 0.1 \times \omega_{01}$. In these superconducting systems, temporarily occupying levels outside the computational subspace offers the key to fast and efficient multi-qubit operations such as conditional-phase [9, 10] and Toffoli gates [11, 12], and high-fidelity single-shot readout [13].

The benefits of using multi-level structures for quantum computing are balanced by more challenging single-qubit control. When driving an individual effective qubit with a resonant pulse at ω_{01} , the anharmonicity $|\Delta|$ imposes a practical limit on the maximum speed of gate operations, marking the transition from decoherence-to leakage-dominated errors. While theoretical optimal control has broken the speed limit using non-analytic pulses [14], analytic pulses with few tuning parameters are preferred by experimentalists for ease of implementation and tuning. Keeping leakage-induced errors below the 1% fault-tolerance threshold of modern error-correcting schemes [15] imposes the necessary but insufficient condition $t_g \gtrsim 2\pi/|\Delta|$ on the single-qubit gate time t_g . Interestingly, the standard Gaussian envelope is insufficient despite satisfying the minimal time-frequency uncertainty product. Proposed [14, 16, 17] DRAG (Derivative Removal by Adiabatic Gate) pulses combining Gaussian and derivative-of-Gaussian envelopes on the in- and out-of-phase quadratures have been widely adopted following validation with phase [18] and transmon [19] qubits in one- and two-qubit devices. To date, the com-

bination of DRAG and improved coherence has achieved average single-qubit gate errors of 0.08% in transmon qubits [20].

Moving forward, it is imperative to preserve high-quality single-qubit control as more effective qubits are crowded in a fixed frequency range. In architectures such as 2D [21] and 3D [22] circuit QED which exploit a common feedline or coupled resonator to drive multiple qubits, control drives couple almost equally to addressed and unaddressed qubits. In this regime of near-unity cross-talk, the absolute detuning $|\delta|$ between the logical transition of one qubit and the leakage transition of its frequency neighbor sets an even lower speed limit when $|\delta| < |\Delta|$. In order to ease coherence time requirements, it is therefore important to design analytic pulses with $t_g \sim 2\pi/|\delta|$ which avoid leakage in both the addressed qubit and its neighbor (henceforth termed internal and external leakage). To this end, Schutjens *et al.* [23] have recently developed Wah-Wah control (Weak AnHarmonicicity With Average Hamiltonian), combining DRAG with sideband modulation in a four-parameter pulse.

In this article, we present the experimental validation of leakage-avoiding Wah-Wah control at the speed limit of a multi-transmon 2D circuit QED processor. We create a bias condition with $\delta/2\pi = 57$ MHz and demonstrate avoidance of both external and internal leakage at gate times $16 \text{ ns} \leq t_g \leq 24 \text{ ns}$. Stroboscopic population measurements show that DRAG-only pulsing induces significant net population in the third level of the unaddressed transmon, while Wah-Wah ensures all population returns to the computational subspace by the end of the pulse. Using a variant of standard randomized benchmarking [24], we show alternating individual control of both qubits with 0.8 – 1.0% average error per computational step. Finally, we use quantum process tomography to demonstrate decoherence-limited idling of the unaddressed qubit as the other undergoes a Wah-Wah pulse train. Optimization of the four-parameter, analytic Wah-Wah pulse shape is straightforward and accelerated

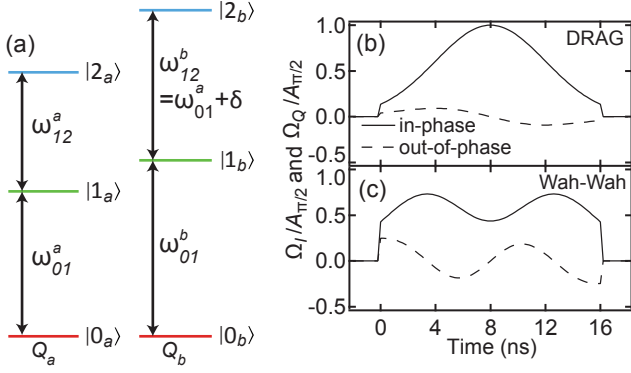


FIG. 1. (color online). (a) Energy level diagram for transmons Q_a and Q_b (not to scale). The ground $|0_k\rangle$ and first-excited $|1_k\rangle$ states of Q_k define a qubit subspace. The Q_a qubit transition frequency and the Q_b leakage transition frequency differ by $\delta = \omega_{12}^b - \omega_{01}^a = 2\pi \times 57$ MHz. (b-c) Comparison of in- and out-of-phase quadrature envelopes Ω_I and Ω_Q , respectively, for optimized DRAG and Wah-Wah $\pi/2$ pulses on Q_a (gate time $t_g = 16$ ns). For DRAG (b), Ω_I and Ω_Q are Gaussian and derivative-of-Gaussian, respectively [Eqs. (1)-(2) with $\sigma = 4$ ns, $A_m = 0$, $\beta = 0.6$ ns]. For Wah-Wah (c), $A_m = 0.9$, $\omega_m/2\pi = 25$ MHz, $\beta = 1.85$ ns.

by a simple model of the system Hamiltonian using independently measured parameters. Our results establish Wah-Wah control as an important tool for scalability, allowing control of frequency-crowded effective qubits at threshold without dedicated control lines.

We focus on two transmons (Q_a and Q_b) within a four-transmon, five-resonator 2D cQED processor of similar design to that of Ref. 25. Resonant control and readout pulses for all qubits are applied via one feedline coupling to readout resonators connecting to one qubit each. Using local flux control, we bias Q_a and Q_b to logical transitions $(\omega_{01}^a, \omega_{01}^b)/2\pi = (6.347, 6.750)$ GHz, and corresponding leakage transitions $(\omega_{12}^a, \omega_{12}^b)/2\pi = (5.980, 6.404)$ GHz, making $\delta = \omega_{12}^b - \omega_{01}^a = 2\pi \times 57$ MHz [Fig. 1(a)]. Thus, we expect [23] DRAG pulses [Fig. 1(b)] targeting Q_a to induce significant leakage from $|1_b\rangle$ to $|2_b\rangle$ for $t_g \lesssim 2\pi/\delta \sim 20$ ns. Indeed, we note that just four back-to-back Q_a DRAG π pulses already leak $\sim 50\%$ of the initial population in $|1_b\rangle$ to $|2_b\rangle$ for $t_g = 16$ ns (Fig. 2). Note that to within the few-percent accuracy limited by state preparation and measurement errors (SPAM), DRAG pulses do successfully avoid internal leakage in Q_a , as expected [14].

Using similar measurements, we now attempt to also avoid external leakage using the additional sideband modulation characteristic of Wah-Wah pulse envelopes [Fig. 1(c)] [23]:

$$\Omega_I(t) = A_\theta e^{-(t - \frac{t_g}{2})^2 / (2\sigma^2)} \left[1 - A_m \cos \left(\omega_m \left(t - \frac{t_g}{2} \right) \right) \right] \quad (1)$$

$$\Omega_Q(t) = \beta \dot{\Omega}_I(t). \quad (2)$$

Here, Ω_I and Ω_Q are the pulse envelopes in the in- and out-of-phase quadratures, and amplitude A_θ determines the rotation angle θ . The theory predicts that sideband modulation of the conventional Gaussian envelope in Ω_I can mitigate external leakage for suitably chosen modulation amplitude A_m and frequency ω_m . Just as in DRAG, keeping Ω_Q proportional to the time derivative of Ω_I should prevent internal leakage in Q_a upon optimizing the scaling parameter β . Figure 2 provides the experimental confirmation of external and internal leakage mitigation to within the accuracy allowed by SPAM. Q_a Wah-Wah π pulses with manually-optimized A_m , ω_m , A_π , and β populate $|2_b\rangle$ only temporarily, returning all population to $|1_b\rangle$ by the end of each pulse. (Details of the Wah-Wah pulse tune-up procedure are provided in the Supplement [26]). A numerical simulation of the system dynamics, which truncates the Hamiltonian at three levels per transmon, shows good correspondence with the manually optimized pulse parameters. To test its utility, we used the simulation to obtain first estimates of pulse parameters at two other Q_b bias points with even tighter separation of their logical frequencies ($\delta/2\pi = -60$ MHz and -80 MHz). We also obtained similar internal and external leakage mitigation for $t_g = 16$ ns (data not shown).

While Wah-Wah pulsing on Q_a successfully mitigates net leakage in Q_b , the temporary excursion of quantum amplitude from $|1_b\rangle$ to $|2_b\rangle$ induces a relative phase between levels $|0_b\rangle$ and $|1_b\rangle$, i.e., a z rotation in the Q_b qubit subspace. This induced phase is a deterministic function of the Q_a pulse parameters defined above. Thus, we can compensate it already in pulse synthesis by adjusting the phase of all subsequent Q_b pulses, in the style of virtual z gates [27]. To calibrate the phase shift, we embed several consecutive Wah-Wah Q_a pulses (either all π or $\pi/2$) into the second wait period in a standard echo sequence on Q_b ($\pi/2$, wait, π , wait, $\pi/2$). The final $\pi/2$ rotation translates the acquired phase into a population difference between $|0_b\rangle$ and $|1_b\rangle$. We observe that the induced Q_b phase is independent of rotation axis and linear in the number of Q_a pulses of a given type: 8.2° (38°) per $\pi/2$ (π) pulse. We perform a similar calibration of compensating z gates on Q_a for DRAG pulses applied to Q_b . Even though $(\omega_{12}^a - \omega_{01}^b)/2\pi = -770$ MHz and Q_b DRAG pulsing does not produce Q_a leakage (shown below), there is phase accrual in the Q_a qubit subspace: 2.5° (9.3°) per $\pi/2$ (π) pulse.

In order to test both leakage mitigation and phase compensation to higher accuracy than allowed by SPAM, we employ randomized benchmarking (RB). The single-qubit protocol first proposed and implemented by Knill *et al.* [24] (standard RB) provides a valuable baseline for gate errors on the addressed qubit, without concern for the unaddressed one. In standard RB [24, 28], one applies pseudo-random sequences of consecutive π and $\pi/2$ pulses to Q_k and measures the decay of fidelity to the

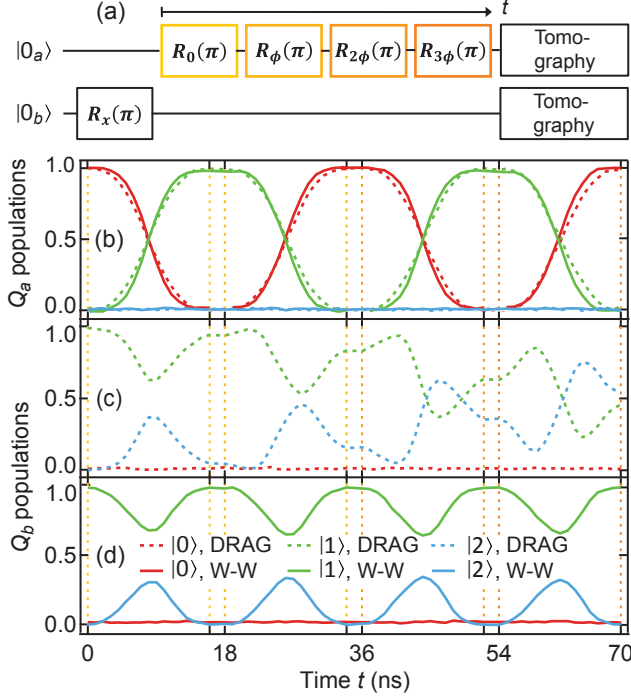


FIG. 2. (color online). Measured evolution of level populations in Q_a and Q_b during four consecutive Q_a π pulses with either DRAG and Wah-Wah envelopes ($t_g = 16$ ns). (a) Pulse sequence. Pulses are separated by a $t_b = 2$ ns buffer. Level populations at time t are obtained by truncating any ongoing Q_a pulse and commencing tomographic operations after a buffer time t_b . (b) Evolution of Q_a levels. Neither DRAG (dashed curves) nor Wah-Wah (solid curves) pulses drive the leakage transition in Q_a . (c-d) Evolution of Q_b levels during DRAG (c) and Wah-Wah (d) Q_a pulses. DRAG pulsing drives the Q_b leakage transition. The chosen relative phase $\phi = 237^\circ$ between subsequent π pulses exacerbates the net leakage. In contrast, Wah-Wah pulses populate $|2_b\rangle$ temporarily, returning the population to $|1_b\rangle$ by the end of each pulse.

ideal final state of that qubit (always $|0_k\rangle$ or $|1_k\rangle$) as the number of pulses is increased [Fig. 3(a)]. This decay allows extracting [26, 29] the average error per computational step (EPS), where computational step is defined as a pair of back-to-back π and $\pi/2$ pulses [24]. We extract EPS as a function of the step time $t_s = 2(t_g + t_b)$ by varying the buffer time t_b between pulses ($t_b \geq 2$ ns). To within statistical error, a linear fit of $\text{EPS}(t_s)$ for Q_a (Q_b) at short t_s extrapolates to the origin [Figs. 3(b)-(c)]. This observation suggests that the minimal 0.4% (0.4%) EPS is already decoherence limited.

With the EPS baselines from standard RB in place, we now employ alternating RB to investigate whether control of either qubit can remain decoherence limited when pulses are interleaved on the other. We apply an RB pulse on one qubit during the buffer ($t_b \geq t_g + 4$ ns) for the other, and perform virtual z -gate compensation

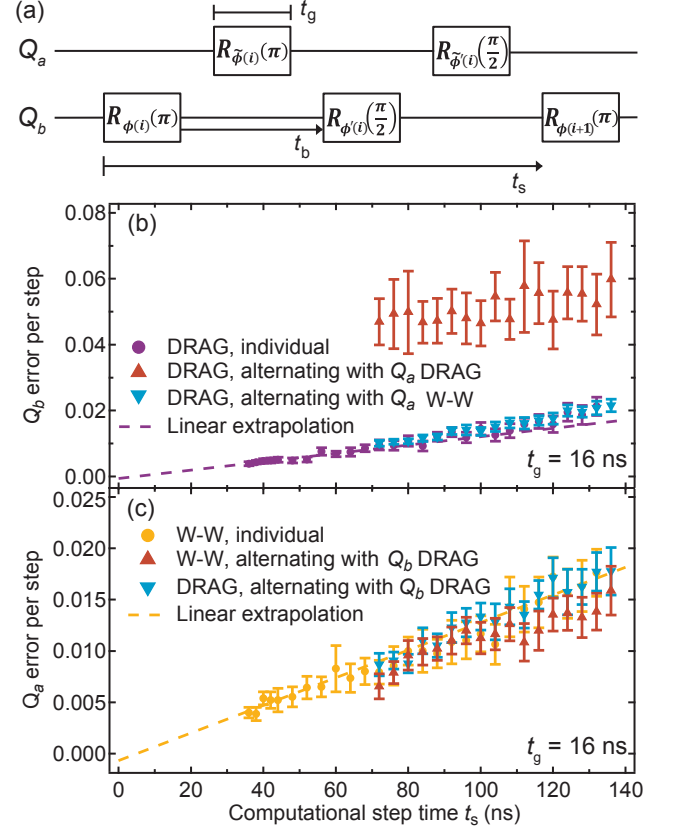


FIG. 3. (color online). Demonstration of decoherence-limited single-qubit control via individual and alternating randomized benchmarking. (a) Pseudo-random control pulses are applied to either one transmon or to both in alternating fashion. The average error per computational step (EPS) is extracted as a function of the computational step time $t_s = 2t_g + 2t_b$ (without and with a symmetrically timed RB pulse on the other transmon during buffer). (b) EPS for optimized Q_b DRAG pulses. The linear t_s dependence observed without Q_a pulses extrapolates to $(-6 \pm 9) \times 10^{-4}$ at $t_s = 0$, indicating decoherence-limited control. The fits are done to the first ten data points. The alternating EPS matches the individual EPS for Q_a Wah-Wah. In contrast, alternating with Q_a DRAG pulsing worsens the EPS to $\sim 5\%$. The large error bars reflect high sensitivity of $|2_b\rangle$ leakage to the particular sequence of Q_a rotations within the randomization. (c) EPS for optimized Q_a DRAG and Wah-Wah pulses. Overlapping results are obtained without and with alternating RB DRAG pulses on Q_b . The observed linear t_s dependence of EPS extrapolates to $(-7 \pm 9) \times 10^{-4}$ at $t_s = 0$, indicating that Q_a control is also decoherence limited.

for all pulses. Alternating RB performed with DRAG pulses on both Q_a and Q_b has no impact on Q_a , but increases the Q_b EPS to $\sim 5\%$ [Fig. 3(b)]. However, by using Wah-Wah pulses on Q_a , we recover the decoherence limited baselines simultaneously on both qubits. Similar results for $t_g = 20$ ns and 24 ns are presented in the Supplement [26].

As the final test of whether Wah-Wah pulsing on Q_a

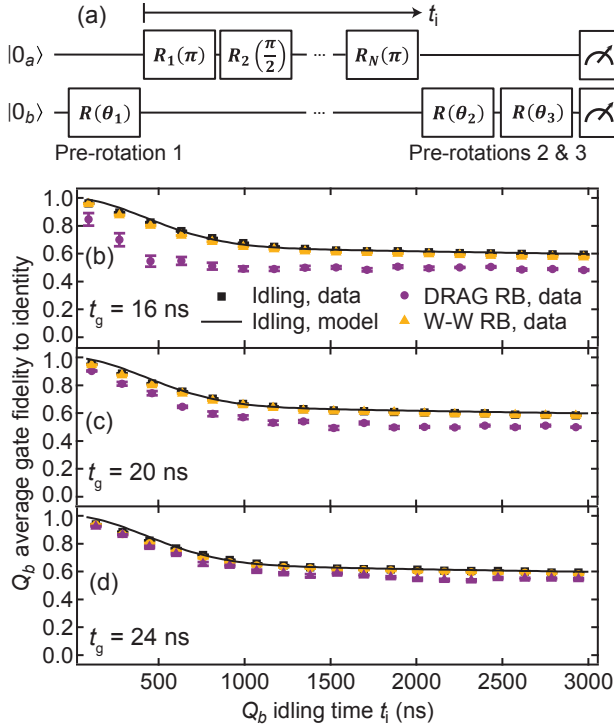


FIG. 4. (color online). Q_b average gate fidelity to the identity operation during various types of idling: no Q_a pulsing, Q_a DRAG RB, and Q_a Wah-Wah RB. (a) Pulse sequence. Initial and final rotations on Q_b are used for QPT of the evolution of Q_b qubit state to the three-level subspace. Results are shown for gate times (b) $t_g = 16$ ns, (c) 20 ns, and (d) 24 ns ($t_b = 2$ ns fixed). Model curves for true idling take into account the measured Q_b qubit relaxation and dephasing times [26]. The model assumes dephasing dominated by $1/f$ noise [30]. The Q_b average gate fidelity to identity during Q_a Wah-Wah RB (circles) is indistinguishable from that of true idling. In contrast, Q_a DRAG RB (triangles) deteriorates fidelity at shorter t_i .

affects Q_b , we perform quantum process tomography (QPT) of Q_b under various idling conditions: no pulses on Q_a (true idling), Q_a DRAG RB, and Q_a Wah-Wah RB (Fig. 4). The process map is a 9×4 transfer matrix [31] relating an initial reduced density matrix in the Q_b qubit subspace to a final reduced density matrix in the three-level [32] subspace. The Q_b average gate fidelity to identity for true idling decreases consistently with an analytic model [26] based on measured Q_b relaxation and dephasing rates. As expected, Q_b idling is compromised under Q_a DRAG RB, and worsens the shorter t_g . An analysis discerning contributions from population transfer and dephasing errors [26] confirms that the loss of idling fidelity is limited by induced leakage and not by imperfect z -gate compensation. Remarkably, the idling fidelity under Q_a Wah-Wah RB is nearly identical to the true idling fidelity for all t_g , further demonstrating the usefulness of the new control method.

In summary, we have shown experimentally, using level-population measurements, RB, and QPT, that Wah-Wah control [23] successfully mitigates crosstalk-induced leakage in a crowded spectrum of transmon qubits at gate times where the widely-adopted DRAG control fails. Wah-Wah control therefore represents a step towards scalability in multi-qubit architectures by allowing selective control of an increasing number of effective qubits without an equal addition of control lines. Wah-Wah builds sideband modulation to DRAG without sacrificing the analytic nature of the two-quadrature pulse shape, adding only two easily optimized parameters. Our demonstration in circuit QED takes place in the worst-case regime of unity crosstalk, with control pulses applied via one common feedline coupling equally to the addressed qubit and the unaddressed nearest-frequency neighbor. Looking forwards, as two-qubit gate and measurement times [33] decrease to that of single-qubit gates, the current restriction to non-overlapping control of frequency-neighboring qubits could ultimately bottleneck the clock cycle in surface-code quantum error correction [15]. A useful generalization of Wah-Wah, however, would allow simultaneous control of two qubits at small $|\delta|$.

We thank D. J. Egger, R. Schutjens and F. K. Wilhelm for many helpful discussions, N. K. Langford and D. Ristè for helpful comments on the manuscript, and D. J. Thoen and T. M. Klapwijk for NbTiN thin films. This work is funded by EU FP7 project SCALEQIT, the Netherlands Organization for Scientific Research (NWO, VIDI scheme), and a Marie Curie Career Integration Grant. V.V. was supported by the Research Foundation of Helsinki University of Technology.

-
- [1] T. D. Ladd, F. Jelezko, R. Laflamme, Y. Nakamura, C. Monroe, and J. L. O'Brien, *Nature*, **464**, 45 (2010).
 - [2] R. Hanson and D. D. Awschalom, *Nature*, **453**, 1043 (2008).
 - [3] C. Monroe and J. Kim, **339**, 1164 (2013).
 - [4] B. P. Lanyon, *et al.*, *Nature Phys.*, **5**, 134 (2009).
 - [5] M. H. Devoret and R. J. Schoelkopf, *Science*, **339**, 1169 (2013).
 - [6] J. Koch, *et al.*, *Phys. Rev. A*, **76**, 042319 (2007).
 - [7] J. M. Martinis, S. Nam, J. Aumentado, and C. Urbina, *Phys. Rev. Lett.*, **89**, 117901 (2002).
 - [8] M. Steffen, S. Kumar, D. P. DiVincenzo, J. R. Rozen, G. A. Keefe, M. B. Rothwell, and M. B. Ketchen, *Phys. Rev. Lett.*, **105**, 100502 (2010).
 - [9] F. W. Strauch, P. R. Johnson, A. J. Dragt, C. J. Lobb, J. R. Anderson, and F. C. Wellstood, *Phys. Rev. Lett.*, **91**, 167005 (2003).
 - [10] L. DiCarlo, *et al.*, *Nature*, **460**, 240 (2009).
 - [11] A. Fedorov, L. Steffen, M. Baur, M. P. da Silva, and A. Wallraff, *Nature*, **481**, 170 (2012).
 - [12] M. D. Reed, L. DiCarlo, S. E. Nigg, L. Sun, L. Frunzio, S. M. Girvin, and R. J. Schoelkopf, *Nature*, **482**, 382

- (2012).
- [13] F. Mallet, F. R. Ong, A. Palacios-Laloy, F. Nguyen, P. Bertet, D. Vion, and D. Esteve, *Nature Phys.*, **5**, 791 (2009).
 - [14] F. Motzoi, J. M. Gambetta, P. Rebentrost, and F. K. Wilhelm, *Phys. Rev. Lett.*, **103**, 110501 (2009).
 - [15] A. G. Fowler, M. Mariantoni, J. M. Martinis, and A. N. Cleland, *Phys. Rev. A*, **86**, 032324 (2012).
 - [16] J. M. Gambetta, F. Motzoi, S. T. Merkel, and F. K. Wilhelm, *Phys. Rev. A*, **83**, 012308 (2011).
 - [17] F. Motzoi and F. K. Wilhelm, *Phys. Rev. A*, **88**, 062318 (2013).
 - [18] E. Lucero, *et al.*, *Phys. Rev. A*, **82**, 042339 (2010).
 - [19] J. M. Chow, L. DiCarlo, J. M. Gambetta, F. Motzoi, L. Frunzio, S. M. Girvin, and R. J. Schoelkopf, *Phys. Rev. A*, **82**, 040305 (2010).
 - [20] R. Barends, *et al.*, *Nature*, **508**, 500 (2014).
 - [21] A. Wallraff, D. I. Schuster, A. Blais, L. Frunzio, R.-S. Huang, J. Majer, S. Kumar, S. M. Girvin, and R. J. Schoelkopf, *Nature*, **431**, 162 (2004).
 - [22] H. Paik, *et al.*, *Phys. Rev. Lett.*, **107**, 240501 (2011).
 - [23] R. Schutjens, F. Abu Dagga, D. J. Egger, and F. K. Wilhelm, *Phys. Rev. A*, **88**, 052330 (2013).
 - [24] E. Knill, *et al.*, *Phys. Rev. A*, **77**, 012307 (2008).
 - [25] O.-P. Saira, J. P. Groen, J. Cramer, M. Meretska, G. de Lange, and L. DiCarlo, *Phys. Rev. Lett.*, **112**, 070502 (2014).
 - [26] See Supplementary Material.
 - [27] M. Steffen, L. M. K. Vandersypen, and I. L. Chuang, *J. Magn. Reson.*, **146**, 369 (2000).
 - [28] J. M. Chow, *et al.*, *Phys. Rev. Lett.*, **102**, 090502 (2009).
 - [29] E. Magesan, J. M. Gambetta, and J. Emerson, *Phys. Rev. A*, **85**, 042311 (2012).
 - [30] F. Yoshihara, K. Harrabi, A. O. Niskanen, Y. Nakamura, and J. S. Tsai, *Phys. Rev. Lett.*, **97**, 167001 (2006).
 - [31] J. M. Chow, *et al.*, *Phys. Rev. Lett.*, **109**, 060501 (2012).
 - [32] R. Bianchetti, S. Filipp, M. Baur, J. Fink, C. Lang, L. Steffen, M. Boissonneault, A. Blais, and A. Wallraff, *Phys. Rev. Lett.*, **105**, 223601 (2010).
 - [33] D. Sank, *et al.*, arXiv:1401.0257 (2014).

Supplement to “Mitigating information leakage in a crowded spectrum of weakly anharmonic qubits”

V. Vesterinen,^{1,2} O.-P. Saira,² A. Bruno,² and L. DiCarlo²

¹ VTT Technical Research Centre of Finland, P.O. Box 1000, 02044 VTT, Finland

² Kavli Institute of Nanoscience, Delft University of Technology,
P.O. Box 5046, 2600 GA Delft, The Netherlands

(Dated: February 23, 2022)

EXPERIMENTAL DETAILS

Device

The chip is a four-transmon, five-resonator 2D cQED quantum processor of nearly identical design and fabrication as that presented in Ref. 1. An optical image of the device and detailed schematic of the setup are shown in Fig. S1. A high- Q resonator bus (5.16 GHz fundamental) couples to every transmon, while dedicated resonators, each dispersively coupled to one transmon, allow individual readouts via a common feedline. Transmon transition frequencies are individually controlled by dedicated flux-bias lines, each short-circuited near one transmon SQUID loop. Throughout this experiment, Q_a was biased at its flux-insensitive point, where $\omega_{01}^a/2\pi = 6.347$ GHz and $\Delta_a/2\pi = -357$ MHz. The Q_a readout resonator has a fundamental frequency of $\omega_r^a/2\pi = 7.7042$ GHz (for Q_a in $|0_a\rangle$), a coupling-limited linewidth of $\kappa_a/2\pi = 1.5$ MHz, and a dispersive coupling strength of $\chi_a/\pi = -1.3$ MHz. Three bias points were explored for Q_b (Table S1). The other two (inactive) transmons on the chip were biased at 4.31 GHz and 7.25 GHz throughout.

TABLE S1. Summary of Q_b -related device parameters at the three bias points explored.

| Bias point | 1 | 2 | 3 |
|----------------------------|--------|--------|--------|
| $\omega_{01}^b/2\pi$ (GHz) | 6.750 | 6.636 | 6.616 |
| $\Delta_b/2\pi$ (MHz) | -346 | -349 | -350 |
| $\delta/2\pi$ (MHz) | 57 | -60 | -81 |
| $\omega_r^b/2\pi$ (GHz) | 7.8181 | 7.8178 | 7.8177 |
| $\kappa_b/2\pi$ (MHz) | 1.8 | N.A. | N.A. |
| χ_b/π (MHz) | -1.7 | N.A. | N.A. |

Additional device parameters at bias point 1

For bias point 1, where all shown data were taken, we calibrated several device parameters needed as input for simulation (discussed below). Measured relaxation and dephasing times of Q_a and Q_b are listed in Table S2. The Rabi frequencies of equal-amplitude drives resonant with the $|0\rangle \leftrightarrow |1\rangle$ and $|1\rangle \leftrightarrow |2\rangle$ transitions of each transmon are listed in Table S3, normalized to that of

TABLE S2. Measured qubit relaxation $T_{1(1\rightarrow 0)}$, Ramsey T_2^{Ramsey} , and echo T_2^{echo} times at bias point 1. The measured relaxation time $T_{1(2\rightarrow 1)}$ from second to first excited state in each transmon is also listed.

| Transmon | Q_a | Q_b |
|---|-------|-------|
| $T_{1(1\rightarrow 0)}$ (μs) | 7.65 | 5.65 |
| $T_{1(2\rightarrow 1)}$ (μs) | 4.18 | 3.66 |
| T_2^{Ramsey} (μs) | 2.13 | 0.64 |
| T_2^{echo} (μs) | 2.33 | 1.40 |

TABLE S3. Measured Rabi frequencies for equal-amplitude drives resonant with the $|0_k\rangle \leftrightarrow |1_k\rangle$ and $|1_k\rangle \leftrightarrow |2_k\rangle$ transitions, and estimated coupling strength of the ω_{01}^a drive to the four transitions. All values are normalized to that of the $|0_a\rangle \leftrightarrow |1_a\rangle$ transition.

| Transmon Q_k | Q_a | Q_b |
|--|-------|-------|
| Rabi frequency at ω_{01}^k | 1 | 0.90 |
| Rabi frequency at ω_{12}^k | 1.42 | 1.25 |
| Coupling λ_1^k of ω_{01}^a drive to $ 0_k\rangle \leftrightarrow 1_k\rangle$ | 1 | 0.5 |
| Coupling λ_2^k of ω_{01}^a drive to $ 1_k\rangle \leftrightarrow 2_k\rangle$ | 2.4 | 1.2 |

the $|0_a\rangle \leftrightarrow |1_a\rangle$ transition. From these, we estimate the relative coupling strength of a drive centered at ω_{01}^a to the four transitions by simulating the filter functions of the two readout resonators at ω_{01}^a using Microwave Office.

Transmon readout

Multiplexed readout. Simultaneous, independent readouts of Q_a and Q_b were performed by applying square-envelope tones (1 μs duration) at $\omega_m^a = \omega_r^a + 2\chi_a$ and $\omega_m^b \approx \omega_r^b + 2\chi_b$ to the feedline, respectively. To preserve the phase of measurement tones between experiment repetitions, we ensured that $\omega_m^\Delta = \omega_m^b - \omega_m^a$ was an integer multiple of $2\pi/t_{\text{rep}}$, where $t_{\text{rep}} = 100$ μs is the experiment repetition time. The amplified feedline output was demodulated by an IQ mixer, low-pass filtered (corner frequency 1.2 GHz) and digitized at $\delta t = 1$ ns sampling interval (see Fig. S1 for the complete readout chain). The mixer local oscillator frequency was chosen equal to ω_m^a . The two quadratures for Q_a readout were obtained by filtering the $I[n]$ and $Q[n]$ streams with an averager rejecting all multiples of ω_m^Δ . For Q_b readout,

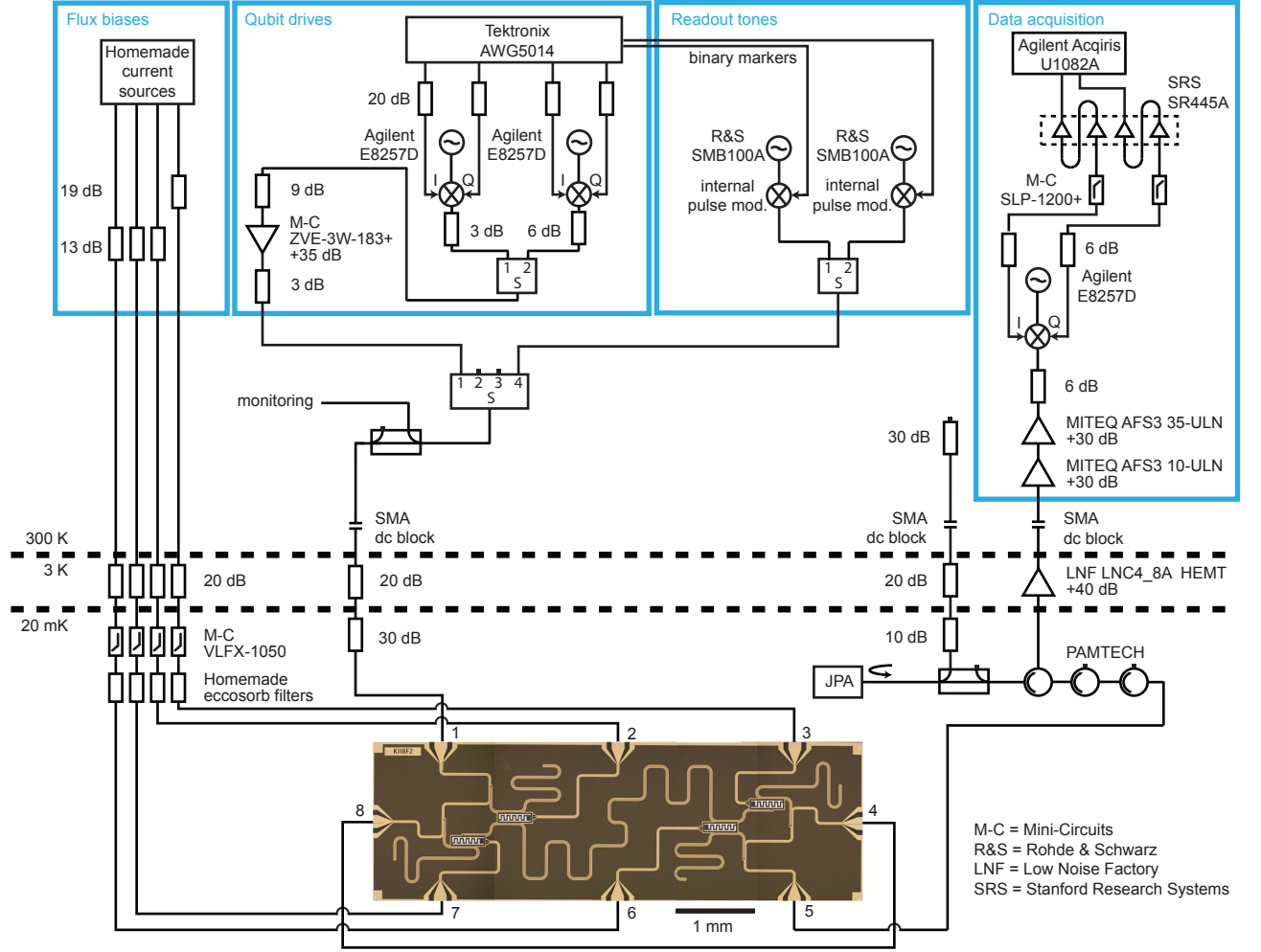


FIG. S1. Device and experimental setup. The 2 mm \times 7 mm chip is cooled to 20 mK in a $^3\text{He}/^4\text{He}$ dilution refrigerator (Leiden Cryogenics CF-450). The chip ports are labeled 1 through 8. Low-pass filtered d.c. currents generating static flux biases for the transmons enter through ports 2 (inactive transmon, transition frequency 4.31 GHz), 3 (Q_a), 6 (also inactive, transition frequency 7.25 GHz), and 7 (Q_b). All microwave control and readout pulses are applied at the single-feedline input port (1). Feedline ports 8 and 4 are externally connected by a short coaxial cable. Transmon readout is performed applying two simultaneous square-envelope pulses (1 μs duration) near the fundamental frequencies of the dedicated resonators coupled to Q_a and Q_b . The transmitted feedline signal exiting at port 5 is routed by circulators (Pamtech) past a Josephson parametric amplifier (JPA, unpumped and unused) and into a HEMT amplifier (Low Noise Factory) at 3 K. Two room-temperature amplifiers (Miteq) further amplify the readout signals, which are subsequently demodulated with an IQ mixer (Marki Microwave). The mixer local oscillator frequency is chosen equal to the measurement frequency of one of the two readout resonators (thus, 0 Hz IF) and is 100 MHz offset from the second. The IF signals are amplified (Stanford Research Systems), digitized (Agilent), and homodyne detected digitally to complete the simultaneous readout of both transmons. DRAG and Wah-Wah pulse envelopes for resonant qubit control are generated by a Tektronix AWG5014 arbitrary waveform generator. We employ ± 50 MHz single-sideband modulation to prevent spurious transmon driving by leakage of the local oscillator in the IQ mixers used for pulse up-conversion.

the two quadratures were derived from $I[n]$ by computing $I[n] \cos(\omega_m^\Delta n \delta t)$ and $I[n] \sin(\omega_m^\Delta n \delta t)$ and filtering with the averager. Finally, these four signals were integrated over the 1 μs interval to obtain the four voltages V_I^a , V_Q^a , V_I^b , and V_Q^b . The single-shot readout fidelities of Q_a and Q_b were 63% and 65%, respectively. We note that the parametric amplifier present in the readout chain was not employed as we did not require high readout fidelity

for this experiment.

Measurement model. We relate the average integrated voltages $\langle V_I^k \rangle$ and $\langle V_Q^k \rangle$ to the level populations of transmon Q_k using the model [2]

$$\langle V_i^k \rangle = \text{Tr}(\rho_k M_i^k),$$

where

$$M_i^k = \beta_{i0}^k \Pi_0^k + \beta_{i1}^k \Pi_1^k + \beta_{i2}^k \Pi_2^k, \quad (\text{S1})$$

$\hat{\Pi}_l^k = |l_k\rangle\langle l_k|$, and ρ_k the reduced qutrit density matrix of Q_k . We calibrate the coefficients $\beta_{i,j}^k$ by measuring $\langle V_i^k \rangle$ immediately after preparing $|0_k\rangle$, $|1_k\rangle$, and $|2_k\rangle$. We prepare the last two states using optimized DRAG pulses $R_{x,01}^k(\pi)$ and $R_{x,12}^k(\pi)R_{x,01}^k(\pi)$, respectively (see below for pulse details). Here, subscripts 01 and 12 indicate rotations in the $\{|0_k\rangle, |1_k\rangle\}$ and $\{|1_k\rangle, |2_k\rangle\}$ subspaces, respectively.

Extraction of level populations. To extract the level populations $P_j^k = \text{Tr}(\rho_k \Pi_j^k)$ in transmon Q_k , we solve the set of three linear equations given by $\langle V_I^k \rangle$, $\langle V_Q^k \rangle$ and the (assumed) constraint $\sum_{i=0}^2 P_j^k = 1$. For the stroboscopic measurements in Figs. 2 and S2, we enhance the accuracy of Q_b level population measurements by increasing the number of linear equations to 7. We measure $\langle V_I^b \rangle$ and $\langle V_Q^b \rangle$ with measurement pre-rotations I , $R_{x,01}^b(\pi)$ and $R_{x,12}^b(\pi)$, and perform unweighted least-squares inversion. Q_a level population measurements in Fig. 2(b) are performed with Q_b pre-rotation I .

Pulse tuning

Tune-up of Q_a and Q_b pulses at each bias point and t_g began with a manual optimization of DRAG pulses on each transmon without concern for their effect on the other. To facilitate the fine tuning of the pulse amplitude A_θ ($A_{\pi/2} = A_\pi/2$) and the DRAG parameter β , we used a test sequence similar to those in Refs. 3 and 4. Each segment of the sequence applies one of 21 different pairs of pulses (each drawn from $\{I, R_{x,01}^k(\pi/2), R_{y,01}^k(\pi/2), R_{x,01}^k(\pi), R_{y,01}^k(\pi)\}$) to $|0_k\rangle$ and immediately performs measurement on Q_k . The pulse pairs are picked and ordered so that the Q_k qubit Bloch vector is ideally left at the north pole, equatorial plane or south pole of the Bloch sphere, in progression. The deviations from a three-level staircase in $\langle V_i^k \rangle$ provide a useful footprint of tune-up errors.

When turning on Wah-Wah pulsing of Q_a at bias point 1, we followed a manual optimization procedure. For each choice of sideband-modulation parameters A_m and ω_m , we first estimated the amplitude needed to preserve the area under the in-phase quadrature envelope. We multiplied the DRAG A_θ by $I_{\text{DRAG}}/(I_{\text{DRAG}} - A_m I_{\text{W-W}})$, where

$$I_{\text{DRAG}} = \int_0^{2\sigma} e^{-t^2/2\sigma^2} dt, \quad (\text{S2})$$

$$I_{\text{W-W}} = \int_0^{2\sigma} e^{-t^2/2\sigma^2} \cos(\omega_m t) dt. \quad (\text{S3})$$

We found this method to be accurate to $\pm 0.4\%$. Using the test sequence above (but implemented with Wah-Wah pulses), we next tuned β . Finally, similarly to Figs. 2 and S2, we measured the P_2^b produced by a sequence of four back-to-back Q_a Wah-Wah pulses. In this

way, we manually found the Wah-Wah parameters (A_θ , β , A_m , and ω_m) pulses that produce minimal P_2^b while performing the intended Q_a operation. The procedure was separately performed for $\theta = \pi$ and $\pi/2$ pulses. Once a good correspondence was established between manually optimized pulse parameters and those suggested by simulation, we increasingly relied on simulation to fix A_m and ω_m , and only manually tuned β . A summary of optimal Q_a DRAG, Q_a Wah-Wah, and Q_b DRAG pulse parameters at the three bias points and several t_g is provided in Table S4.

We finally note that to calibrate DRAG pulses in the $\{|1_k\rangle, |2_k\rangle\}$ subspace, we modified the test sequence to apply a pre-optimized $R_{x,01}^k(\pi)$ before applying the pulse pairs (each drawn from $\{I, R_{x,12}^k(\pi/2), R_{y,12}^k(\pi/2), R_{x,12}^k(\pi), R_{y,12}^k(\pi)\}$). No additional mixers were required for pulse up-conversion as both ω_{01}^k and ω_{12}^k could be reached by single-sideband modulation.

TABLE S4. Parameters of optimized Q_a and Q_b pulses at three bias points.

| | | | Bias point | | |
|-----------------------|---------------------------|-----------------------|------------|--------|------|
| | | | 1 | 2 | 3 |
| $t_g = 16 \text{ ns}$ | W-W $R_{n,01}^a(\pi)$ | A_m | 0.9 | 0.3585 | -0.8 |
| | | $\omega_m/2\pi$ (MHz) | 12.5 | 99.6 | 17.5 |
| | | β (ns) | 0.9 | 0.2 | 0.2 |
| | W-W $R_{n,01}^a(\pi/2)$ | A_m | 0.9 | 0.6743 | 0.5 |
| | | $\omega_m/2\pi$ (MHz) | 25 | 76.5 | 25 |
| | | β (ns) | 1.85 | 0.2 | 0.3 |
| | DRAG $R_{n,01}^a(\theta)$ | β (ns) | 0.6 | 0.2 | 0.2 |
| | DRAG $R_{n,01}^b(\theta)$ | β (ns) | 0.7 | -0.1 | -0.1 |
| $t_g = 20 \text{ ns}$ | W-W $R_{n,01}^a(\pi)$ | A_m | 0.23 | | |
| | | $\omega_m/2\pi$ (MHz) | 13.8 | | |
| | | β (ns) | 0.62 | | |
| | W-W $R_{n,01}^a(\pi/2)$ | A_m | 0.68 | | |
| | | $\omega_m/2\pi$ (MHz) | 23.8 | | |
| | | β (ns) | 0.95 | | |
| $t_g = 24 \text{ ns}$ | W-W $R_{n,01}^a(\pi)$ | A_m | -0.65 | | |
| | | $\omega_m/2\pi$ (MHz) | 15 | | |
| | | β (ns) | 0.6 | | |
| | W-W $R_{n,01}^a(\pi/2)$ | A_m | 0.45 | | |
| | | $\omega_m/2\pi$ (MHz) | 22.5 | | |
| | | β (ns) | 0.7 | | |
| | DRAG $R_{n,01}^a(\theta)$ | β (ns) | 0.6 | | |
| | DRAG $R_{n,01}^b(\theta)$ | β (ns) | 0.7 | | |

Randomized benchmarking

The performance of optimized pulses was measured using randomized benchmarking (RB). In standard RB, random pairs of π and $\pi/2$ pulses are applied, all targeting the same transmon. The last $\pi/2$ pulse is chosen so that the targeted transmon ideally ends in either $|0\rangle$ or $|1\rangle$. For some sequences, this involves replacing the last $\pi/2$ with identity. The fidelity \mathcal{F} (squared overlap) of the final transmon state to the ideal final state is measured for each RB sequence. The average $\overline{\mathcal{F}}$ over all RB sequences is then plotted as function of the number of $\pi/2$ pulses, $N_{\pi/2}$.

In alternating RB, two standard RB sequences targeting different transmons are interleaved. Pulses targeting one transmon are applied during the buffer separating pulses targeting the other. Calibrated virtual z gates are applied both ways: to Q_a following a pulse on Q_b , and viceversa.

Pulse randomization. We briefly describe the pulse randomization procedure used to generate RB sequences. We first create at least 5 pseudo-random trains of $\pm\pi/2$ pulses around x and y (both signs and axes with equal probability), with enough pulses that the complete RB sequence would span 4 μs . Each $\pi/2$ pulse train is then interleaved with a train of $N_{\pi/2} + 1$ Pauli randomization pulses. Each Pauli randomization pulse is taken from the set $\{I, R_{x,01}^k(\pi), R_{x,01}^k(-\pi), R_{y,01}^k(\pi), R_{y,01}^k(-\pi)\}$ with equal probability $1/5$. We generate eight randomizations of the Pauli pulse train. Thus, interleaving the $\pi/2$ and Pauli pulse trains produces at least $5 \times 8 = 40$ RB sequences. After the experiment, we learned that the proper choice of Pauli randomization set would have been

$$\{I, R_{x,01}^k(\pi), R_{x,01}^k(-\pi), R_{y,01}^k(\pi), R_{y,01}^k(-\pi), R_{z,01}^k(\pi), R_{z,01}^k(-\pi)\},$$

with probability $1/4$ for I and $1/8$ for all others, and z -axis π rotations replaced with virtual z gates.

Extraction of average error per computational step. Following Ref. 5, we define a computational step as a pair of π and $\pi/2$ pulses including buffers [total step time $t_s = 2(t_g + t_b)$]. Our estimate of the average error per computational step, EPS, is obtained from a fit of $\overline{\mathcal{F}}(N_{\pi/2})$. In the absence of leakage, we expect [5, 6]

$$\overline{\mathcal{F}}(N_{\pi/2}) = (1 - A)e^{-\alpha N_{\pi/2}} + A,$$

with $A = 1/2$ and $\text{EPS} = (1 - e^{-\alpha})/2$. Note that $\overline{\mathcal{F}}(0) = 1$ because we correct for readout errors. This functional form fits very well the $\overline{\mathcal{F}}(N_{\pi/2})$ data for standard RB and for alternating RB with Q_a Wah-Wah pulses, with best-fit asymptotic fidelity $A = 0.50 \pm 0.05$ in all cases. EPS error bars in Figs. 3 and S4 represent 95% confidence intervals.

In the presence of leakage, we expect [7]

$$\overline{\mathcal{F}}(N_{\pi/2}) = \frac{1}{2}e^{-\alpha N_{\pi/2}} + \left(\frac{1}{2} - A\right)e^{-\gamma N_{\pi/2}} + A,$$

with reduced asymptotic fidelity $1/3 \leq A < 1/2$. We find good fits of this form to the Q_b $\overline{\mathcal{F}}$ data for alternating RB with Q_a DRAG pulses. For $t_g = 16$ ns, $t_s = 36$ ns, the best-fit $A = 0.33 \pm 0.02$ confirms strong leakage. Following Ref. 7, we use $(1 - e^{-\alpha})/2$ as estimator of EPS also in this case.

Quantum process tomography

We performed quantum process tomography (QPT) to fully characterize the evolution of Q_b under three idling scenarios: no applied pulses on Q_a , Q_a DRAG RB pulsing, and Q_a Wah-Wah RB pulsing.

In general, a quantum process is a linear, trace-preserving map of density matrices. The channel can be fully described by a transfer matrix \mathcal{R} connecting the input and output density matrices, each expanded in a suitable basis. The Pauli basis is a standard choice for processes confined to a qubit subspace [8]. In our case, the input and output spaces are the qubit and qutrit subspaces of Q_b . For the input space, we use the basis

$$P_1^{(2)} = \begin{pmatrix} 1 & 0 \\ 0 & 0 \end{pmatrix}, \quad P_2^{(2)} = \begin{pmatrix} 0 & 0 \\ 0 & 1 \end{pmatrix},$$

$$P_3^{(2)} = \frac{1}{\sqrt{2}} \begin{pmatrix} 0 & 1 \\ 1 & 0 \end{pmatrix}, \quad P_4^{(2)} = \frac{1}{\sqrt{2}} \begin{pmatrix} 0 & -i \\ i & 0 \end{pmatrix}.$$

For the output space, we use

$$P_1^{(3)} = \begin{pmatrix} 1 & 0 & 0 \\ 0 & 0 & 0 \\ 0 & 0 & 0 \end{pmatrix}, \quad P_2^{(3)} = \begin{pmatrix} 0 & 0 & 0 \\ 0 & 1 & 0 \\ 0 & 0 & 0 \end{pmatrix}, \quad P_3^{(3)} = \begin{pmatrix} 0 & 0 & 0 \\ 0 & 0 & 0 \\ 0 & 0 & 1 \end{pmatrix},$$

$$P_4^{(3)} = \frac{1}{\sqrt{2}} \begin{pmatrix} 0 & 1 & 0 \\ 1 & 0 & 0 \\ 0 & 0 & 0 \end{pmatrix}, \quad P_5^{(3)} = \frac{1}{\sqrt{2}} \begin{pmatrix} 0 & -i & 0 \\ i & 0 & 0 \\ 0 & 0 & 0 \end{pmatrix},$$

$$P_6^{(3)} = \frac{1}{\sqrt{2}} \begin{pmatrix} 0 & 0 & 1 \\ 0 & 0 & 0 \\ 1 & 0 & 0 \end{pmatrix}, \quad P_7^{(3)} = \frac{1}{\sqrt{2}} \begin{pmatrix} 0 & 0 & -i \\ 0 & 0 & 0 \\ i & 0 & 0 \end{pmatrix},$$

$$P_8^{(3)} = \frac{1}{\sqrt{2}} \begin{pmatrix} 0 & 0 & 0 \\ 0 & 0 & 1 \\ 0 & 1 & 0 \end{pmatrix}, \quad P_9^{(3)} = \frac{1}{\sqrt{2}} \begin{pmatrix} 0 & 0 & 0 \\ 0 & 0 & -i \\ 0 & i & 0 \end{pmatrix}.$$

The quantum process is fully characterized by a 9×4 real-valued matrix with elements \mathcal{R}_{pq} .

We used a four-step QPT protocol to extract \mathcal{R} for each idling scenario. The steps are: (i) state preparation,

(ii) idling for a time t_i , (iii) measurement pre-rotation, and (iv) measurement.

(i) For state preparation, a calibrated DRAG pulse U_n was applied to $|0_b\rangle$, taken from the set

$$\{I, R_{x,01}^b(\pi), R_{x,01}^b(\pi/2), R_{x,01}^b(-\pi/2), R_{y,01}^b(\pi/2), R_{y,01}^b(-\pi/2)\}.$$

(ii) The Q_a rotations during t_i were chosen according to the RB protocol described above. The QPT protocol was repeated for 64 distinct RB sequences (8 seeds, 8 Pauli randomizations per seed). The transfer matrix \mathcal{R} was computed as an average over these randomizations.

(iii) The measurement pre-rotations V_m on Q_b were chosen from the set

$$\begin{aligned} &\{I, R_{x,01}^b(\pi/2), R_{x,01}^b(-\pi/2), R_{y,01}^b(\pi/2), R_{y,01}^b(-\pi/2), \\ &R_{x,01}^b(\pi), R_{x,12}^b(\pi/2), R_{x,12}^b(-\pi/2), \\ &R_{y,12}^b(\pi/2), R_{y,12}^b(-\pi/2), R_{x,01}^b(\pi)R_{x,12}^b(\pi/2), \\ &R_{x,01}^b(\pi)R_{x,12}^b(-\pi/2), R_{x,01}^b(\pi)R_{y,12}^b(\pi/2), \\ &R_{x,01}^b(\pi)R_{y,12}^b(-\pi/2), R_{x,01}^b(\pi)R_{x,12}^b(\pi)\}. \end{aligned}$$

Optimized DRAG pulses were used to implement all rotations. This set of pre-rotations augments that of Ref. [9] with redundant rotations in order to increase the stability of the inversion.

(iv) Using the dispersive readout described above, we obtain averaged integrated voltages $\langle V_I \rangle$ and $\langle V_Q \rangle$ for each (V_m, U_n) pair.

The averaged measurement $\langle V_i \rangle_{kl}$ for each (V_m, U_n) pair ($6 \times 15 = 90$ pairs total) is related to \mathcal{R} by

$$\langle V_i \rangle_{mn} = \sum_{pq} \mathcal{R}_{pq} \text{Tr}(V_m^\dagger M_i V_m P_p^{(3)}) \langle 0 | U_n^\dagger P_q^{(2)} U_n | 0 \rangle. \quad (\text{S4})$$

Combining all measurements, we arrive at a set of 180 linear equations for the 36 unknown \mathcal{R}_{pq} . We solve this over-determined set of linear equations by unweighted least-squares inversion.

As a measure of idling performance, we extract the average gate fidelity, F_g , of Q_b to identity [10, 11]. We find

$$\begin{aligned} F_g &= \sum_{j=\pm x, \pm y, \pm z} \text{Tr}[\rho_j \mathcal{E}(\rho_j)] \\ &= \frac{\mathcal{R}_{11} + \mathcal{R}_{22} + \mathcal{R}_{43} + \mathcal{R}_{54} - \mathcal{R}_{31} - \mathcal{R}_{32}}{6} + \frac{1}{3}. \end{aligned}$$

To gain further insight into the sources of infidelity, we decompose F_g as

$$F_g = \frac{F_1 + F_2 + 1}{3}, \quad (\text{S5})$$

where $F_1 = \frac{1}{2}(\mathcal{R}_{11} + \mathcal{R}_{22} - \mathcal{R}_{31} - \mathcal{R}_{32})$ and $F_2 = \frac{1}{2}(\mathcal{R}_{43} + \mathcal{R}_{54})$. F_1 is sensitive to errors in population

transfer. F_2 is sensitive to population transfer and also to pure dephasing within the qubit subspace. For true idling, we model

$$F_1(t_i) = \frac{1 + e^{-t_i/T_{1(1 \rightarrow 0)}}}{2}, \quad (\text{S6})$$

and

$$F_2(t_i) = e^{-t_i/(2T_{1(1 \rightarrow 0)})} e^{-t_i^2/T_\varphi^2}. \quad (\text{S7})$$

The model F_2 reflects dominant pure dephasing by $1/f$ flux noise, as suggested by a non-exponential Ramsey fringe decay observed for Q_b .

SIMULATION

We perform a numerical simulation of the driven two-qubit system in order to: (a) validate the Wah-Wah modulation parameters manually optimized at bias point 1 and (b) speed-up the optimization of these parameters at other bias points. Following Ref. 12, we model the system Hamiltonian in a frame rotating with a resonant drive at ω_{01}^a , truncate at three lowest-energy levels per transmon, and make the rotating wave approximation:

$$\begin{aligned} \hat{H}/\hbar &= \Delta_a \hat{\Pi}_2^a + (\delta - \Delta_b) \hat{\Pi}_1^b + \delta \hat{\Pi}_2^b \\ &+ \frac{\Omega_I(t)}{2} [\lambda_1^a \hat{\sigma}_{x,1}^a + \lambda_1^b \hat{\sigma}_{x,1}^b + \lambda_2^a \hat{\sigma}_{x,2}^a + \lambda_2^b \hat{\sigma}_{x,2}^b] \\ &+ \frac{\Omega_Q(t)}{2} [\lambda_1^a \hat{\sigma}_{y,1}^a + \lambda_1^b \hat{\sigma}_{y,1}^b + \lambda_2^a \hat{\sigma}_{y,2}^a + \lambda_2^b \hat{\sigma}_{y,2}^b]. \end{aligned} \quad (\text{S8})$$

Here, $\sigma_{x,l}^k = |l_k\rangle \langle l-1_k| + |l-1_k\rangle \langle l_k|$, and $\sigma_{y,l}^k = i|l_k\rangle \langle l-1_k| - i|l-1_k\rangle \langle l_k|$. As defined in the main text, $\Delta_k = \omega_{12}^k - \omega_{01}^k$, $\delta = \omega_{12}^b - \omega_{01}^a$, and $\Omega_I(t)$ and $\Omega_Q(t)$ are the in- and out-of-phase pulse envelopes. Finally, λ_l^k is the coupling strength of the drive to the $|l-1_k\rangle \leftrightarrow |l_k\rangle$ transition. All model parameters are obtained from calibration measurements.

For each choice of gate time t_g , bias point, and Q_a pulse rotation angle $\theta \in \{\pi, \pi/2\}$, we identify a manifold of $(A_\theta, \beta, A_m, \omega_m)$ values performing a high-quality pulse on Q_a . For each (A_m, ω_m) pair in the range $A_m \in [-1, 1]$ and $\omega_m/2\pi \in [0, 100 \text{ MHz}]$, we find the A_θ and β achieving the desired rotation angle θ and minimizing internal leakage in Q_a . We then calculate the leakage P_2^b induced by four back-to-back Q_a pulses, starting from $(|0_b\rangle + i|1_b\rangle)/\sqrt{2}$. Similarly to Fig. 2, the phase of these Q_a pulses is increased in progression ($\phi, 2\phi, 3\phi$, and 4ϕ). We repeat for 200 values of ϕ between 0 and 2π . The simulation output consists of an image plot of $\max_\phi P_2^b$ as a function of A_m and ω_m .

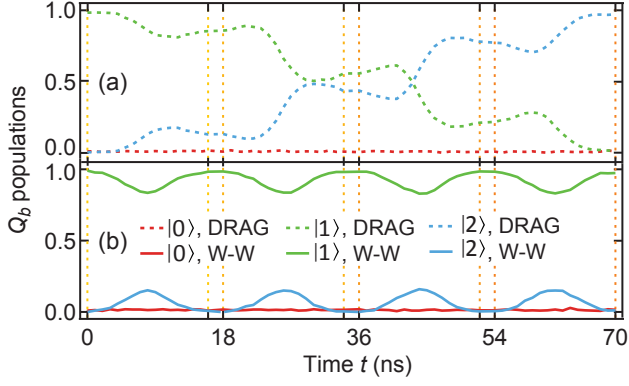


FIG. S2. Measured evolution of Q_b level populations during four back-to-back $\pi/2$ pulses on Q_a , with optimized DRAG and Wah-Wah envelopes ($t_g = 16$ ns). Panels (a) and (b) are dual to Figs. 2(c) and 2(d), respectively, but with $\pi/2$ instead of π pulses on Q_a . The phase of $\pi/2$ pulses is ϕ , 2ϕ , 3ϕ , and 4ϕ , in progression, with $\phi = 319^\circ$.

EXTENDED RESULTS

This section presents four figures lending further support to the main text claims. Complementing Fig. 2, Fig. S2 shows the evolution of level populations in Q_a and Q_b during repeated $\pi/2$ pulses on Q_a . Figure S3 compares measurements and simulation of $|2_b\rangle$ leakage induced by four back-to-back π or $\pi/2$ Wah-Wah pulses on Q_a . Image plots of leakage as a function of modulation parameters show good correspondence between the optimal Wah-Wah parameters found by simulation and

manually in experiment. Complementing Fig. 3, Fig. S4 shows standard and alternating randomized benchmarking results for longer gate times $t_g = 20$ ns and 24 ns. Finally, complementing Fig. 4, Fig. S5 helps identify dominant limitations to Q_b idling from decoherence, leakage error, and phase-compensation error.

- [1] O.-P. Saira, J. P. Groen, J. Cramer, M. Meretska, G. de Lange, and L. DiCarlo, Phys. Rev. Lett., **112**, 070502 (2014).
- [2] S. Filipp, *et al.*, Phys. Rev. Lett., **102**, 200402 (2009).
- [3] J. M. Chow, L. DiCarlo, J. M. Gambetta, A. Nune-kamp, L. S. Bishop, L. Frunzio, M. H. Devoret, S. M. Girvin, and R. J. Schoelkopf, Phys. Rev. A, **81**, 062325 (2010).
- [4] M. Reed, *Entanglement and quantum error correction with superconducting qubits*, PhD Dissertation, Yale University (2013).
- [5] E. Knill, *et al.*, Phys. Rev. A, **77**, 012307 (2008).
- [6] E. Magesan, J. M. Gambetta, and J. Emerson, Phys. Rev. A, **85**, 042311 (2012).
- [7] J. M. Epstein, A. W. Cross, E. Magesan, and J. M. Gambetta, ArXiv:1308.2928 (2013).
- [8] J. M. Chow, *et al.*, Phys. Rev. Lett., **109**, 060501 (2012).
- [9] R. Bianchetti, S. Filipp, M. Baur, J. Fink, C. Lang, L. Steffen, M. Boissonneault, A. Blais, and A. Wallraff, Phys. Rev. Lett., **105**, 223601 (2010).
- [10] A. Gilchrist, N. K. Langford, and M. A. Nielsen, Phys. Rev. A, **71**, 062310 (2005).
- [11] F. Motzoi, J. M. Gambetta, P. Rebentrost, and F. K. Wilhelm, Phys. Rev. Lett., **103**, 110501 (2009).
- [12] R. Schutjens, F. Abu Dagga, D. J. Egger, and F. K. Wilhelm, Phys. Rev. A, **88**, 052330 (2013).

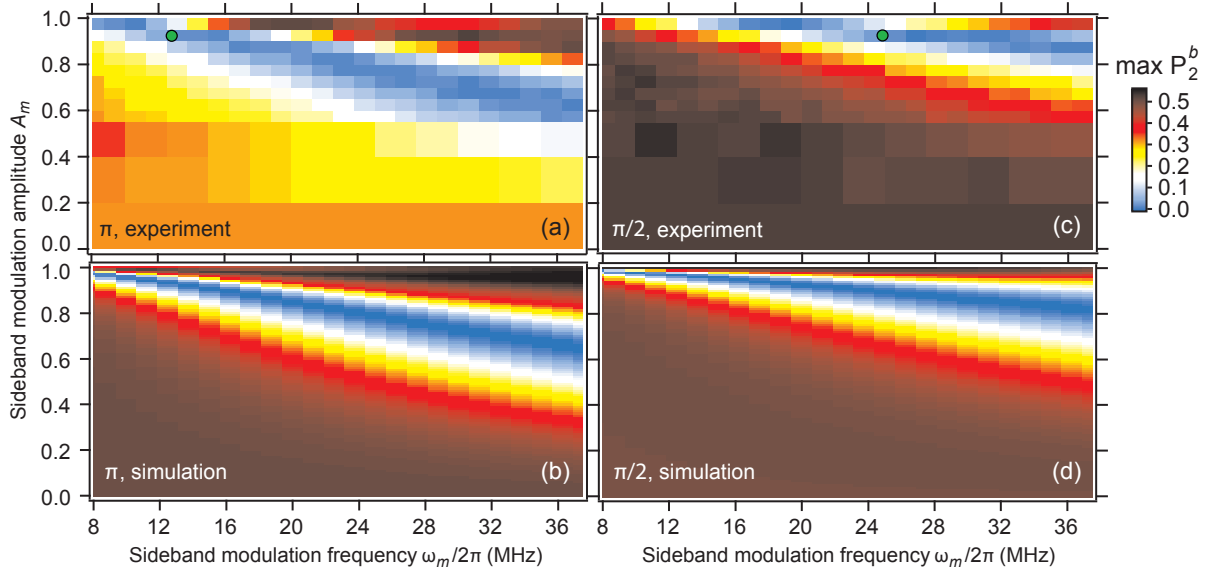


FIG. S3. Image plots of measured (a,c) and simulated (b,d) final population of $|2_b\rangle$, P_2^b , as a function of the modulation parameters A_m and ω_m in four consecutive π (a,b) or $\pi/2$ (c,d) Q_a Wah-Wah pulses ($t_g = 16$ ns). Transmons are initially in $|0_a\rangle$ and $(|0_b\rangle + i|1_b\rangle)/\sqrt{2}$. Similarly to Figs. 2 and S2, the phases of the pulses are ϕ , 2ϕ , 3ϕ , and 4ϕ , in progression. For each (A_m, ω_m) pair, we plot the maximal P_2^b measured over 80 values of ϕ between 0 and 2π . In experiment (a,c), we optimized the β coefficient at the left and right boundaries, and used linear interpolation with respect to ω_m (at fixed A_m) to set β inside. Markers indicate the manually found (A_m, ω_m) pairs minimizing P_2^b in experiment.

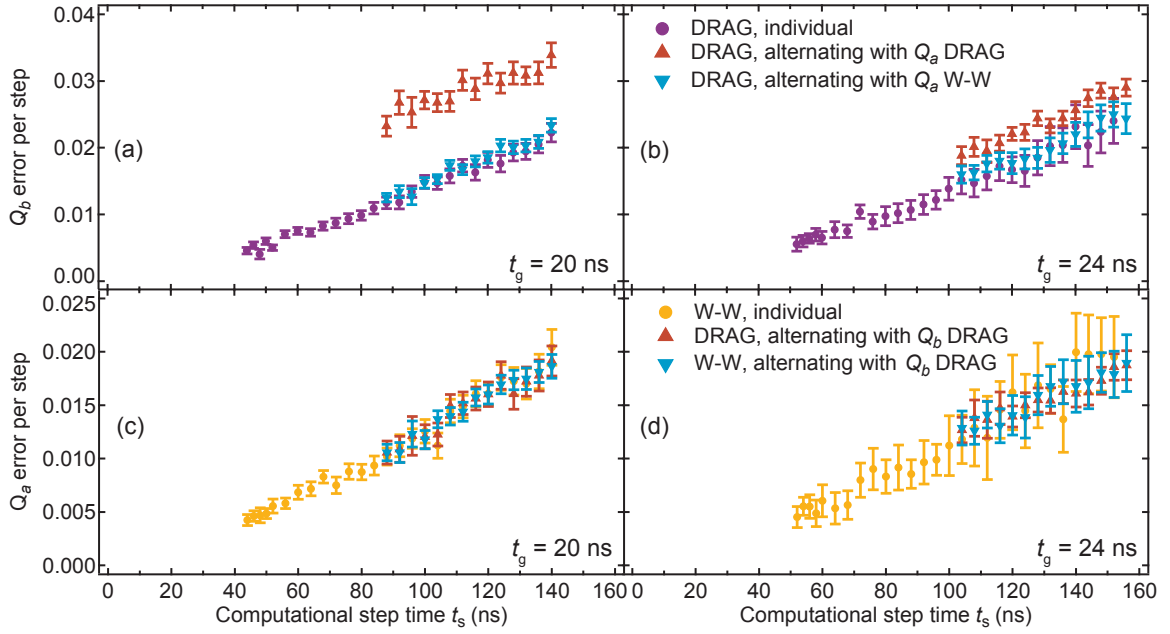


FIG. S4. Error per computational step, EPS, as a function of the computational step time $t_s = 2(t_g + t_b)$, obtained in standard and alternating randomized benchmarking. This figure is dual to Fig. 3, but with gate times $t_g = 20$ ns (a,c) and $t_g = 24$ ns (b,d), corresponding to $t_g|\delta|/2\pi \approx 1.1$ and 1.4 , respectively. As expected, the Q_b leakage induced by Q_a DRAG pulses is less severe the longer t_g . Optimized Q_a Wah-Wah pulsing allows achieving decoherence-limited EPS on Q_b .

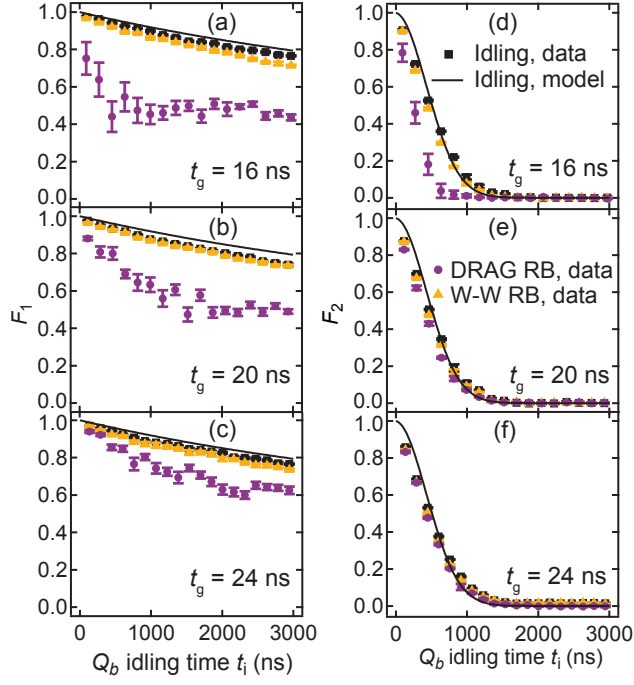


FIG. S5. Q_b average gate fidelity to the identity process as a function of idling time t_i , decomposed into components with different sensitivity to population transfer and to pure dephasing. (a-c) Fidelity F_1 is sensitive to relaxation within the qubit subspace and leakage out of the qubit subspace. (d-f) Fidelity F_2 is also sensitive to pure dephasing within the qubit subspace. Same raw data as in Fig. 4. Squares, circles, and triangles correspond to true idling (i.e., no pulses on Q_a), Q_a DRAG RB, and Q_a Wah-Wah RB, respectively. The combination of these plots allows two conclusions: Q_b idling for Q_a Wah-Wah RB is decoherence limited; Q_b idling for Q_a DRAG RB is dominated by leakage (rather than imperfect z -gate compensation). The large error bars for Q_a DRAG RB reflect the sensitivity of Q_b leakage to the randomization of Q_a DRAG pulses. See text for the details of the model for true idling (solid curves).